



Geometric Properties of Water-ice Clouds as Observed from Jezero Crater in the First 600 sols with the NavCam Instrument On Board the Mars2020 Rover, Perseverance

Priya Patel^{1,2,3} , Leslie Tamppari³, Manuel de la Torre Juárez³, Mark Lemmon⁴ , Andrew Coates^{1,2} , Michael Wolff⁴ , Daniel Toledo⁵, Graziella Branduardi-Raymont^{1,2}, Geraint Jones^{1,2} , Charissa Campbell⁶, John Moores⁶ , Justin Maki³, and Jacqueline Ryan³

¹ Mullard Space Science Laboratory, Dept of Space & Climate Physics, University College London, UK; priya.k.patel.16@ucl.ac.uk

² The Centre for Planetary Sciences at UCL/Birkbeck, London, UK

³ NASA Jet Propulsion Laboratory, California Institute of Technology, USA

⁴ Space Science Institute, USA

⁵ Instituto Nacional de Técnica Aeroespacial (INTA), Madrid, Spain

⁶ York University, Canada

Received 2023 June 20; revised 2023 September 4; accepted 2023 September 13; published 2023 December 4

Abstract

In the first 600 sols of the Mars2020 mission, L_S 5.6° – 316.8°, 46 cloud movies and 145 cloud surveys were collected to observe clouds at Jezero Crater, the landing site of the Perseverance Rover. Cloud movies were processed using the Mean-Frame Subtraction (MFS) method for revealing cloud structures, which were subsequently analyzed using digital-image processing. Two-dimensional Fast Fourier Transforms (2D-FFT) were used to compute cloud structure sizes ranging from 2.90 to 15.25 km for clouds between 30 and 50 km altitude, based on coincident Mars Climate Sounder vertical profiles of atmospheric water-ice. Same-value thresholding was used to detect the cloud structures in MFS-processed and projected cloud movies. The resolution dependence that was needed to resolve these structures over various thresholds was examined to find multifractal scaling of Mars clouds for resolutions between 0.1 and 1.6 km. We characterize the multiscaling observed in the images and its implications for the design of cloud-tracking cameras from the surface as well as for cloud-resolving models.

Unified Astronomy Thesaurus concepts: Planetary science (1255); Planetary atmospheres (1244); Atmospheric clouds (2180); Mars (1007); Rovers (1409)

Supporting material: animations

1. Introduction

The first spacecraft observation of water-ice clouds on Mars was carried out over Arsia Mons by Curran et al. (1973) using the Infrared Interferometer Spectrometer (IRIS) instrument on board the Mariner 9 Orbiter. However, until the mid-1990s it was thought that Mars clouds did not play a significant role in the dynamics of the Martian atmosphere. Through ground-based observations, Clancy et al. (1996) and Clancy & Nair (1996) showed the importance of water-ice clouds in the transport of water as well as their role in radiative processes. Wilson et al. (2008) highlighted that the radiative impact of clouds is essential to account for the atmospheric temperatures observed in the equatorial region. Montmessin (2002) and Madeleine et al. (2012) showed that models are only able to correctly model the water cycle on Mars by factoring in cloud condensation and water-ice microphysics. Kleinböhl et al. (2013) have also shown their role in modulating the amplitude of semidiurnal temperature tides.

Multiple orbiter missions over the last 50 years have studied Martian clouds seasonally and globally. Starting with the Viking Orbiter Infrared Thermal Mapper (IRTM) experiment, Tamppari et al. (2000) and Tamppari et al. (2003) observed water-ice clouds with a peak activity during the northern spring and summer. Furthermore, Mars clouds have been studied using the Mars Color Imager (MARCI; Wolff et al. 2019), Mars Climate

Sounder (MCS; Kleinböhl et al. 2009), and Compact Reconnaissance Imaging Spectrometer for Mars (CRISM; Guzewich et al. 2014) on board the Mars Reconnaissance Orbiter (MRO), the IR mapping spectrometer OMEGA on board Mars Express (Madelaine et al. 2012), and the Mars Orbiter Camera (MOC) and Thermal Emission Spectrometer (TES) on board the Mars Global Surveyor (MGS; Clancy 2003). Specifically, these instruments are used to determine optical depths of cloud and haze, the sizes of ice crystal particles, cloud morphologies, and qualitative classifications.

These global data sets have shown that a belt of water-ice clouds, also known as the aphelion cloud belt (ACB), develops in the equatorial region (10°S–30°N) between solar longitude (L_S) 45° and 140° (Clancy et al. 1996; Tamppari et al. 2000; Smith 2004). The ACB plays a significant role in the seasonal and latitudinal distribution of atmospheric water. It is thought that the ACB limits cross-equatorial water vapor transport in the northern summer, the so-called Hadley circulation (Clancy et al. 1996; Montmessin et al. 2004).

Along with the ACB, the north (NPH) and south (SPH) polar hood clouds are also prevalent on Mars. They are associated with very cold atmospheric temperatures at medium to high latitudes during the fall, winter, and spring seasons (Haberle et al. 2017). Specifically, the NPH has been observed since very early telescopic observations (e.g., Martin et al. 1992), and NPH clouds are prevalent near the edge of the seasonal polar cap in the spring and late summer and early fall, forming the polar hood (e.g., Briggs & Leovy, 1974; Tamppari et al. 2003). Tamppari et al. (2008) show the spatial and seasonal changes of NPH water-ice clouds using data provided by the TES,



Original content from this work may be used under the terms of the [Creative Commons Attribution 4.0 licence](https://creativecommons.org/licenses/by/4.0/). Any further distribution of this work must maintain attribution to the author(s) and the title of the work, journal citation and DOI.

covering nearly three northern spring and summer periods. This data set shows the disappearance of NPH clouds near $L_S = 75^\circ$ and their reappearance near $L_S = 160^\circ$ – 165° (Tamppari et al. 2008).

From orbiter data, we obtain the global characteristics of Mars clouds and understand their seasonal and diurnal patterns. However, it is through gathering data from the surface that we acquire ground-truth measurements of Mars clouds by imaging cloud structures from a closer range and with higher resolution. The early missions, such as Mars Pathfinder (Smith & Lemmon 1999) and the Mars Exploration Rovers (MER; Opportunity and Spirit) studied clouds using imagery. Opportunity, for example, acquired images of water-ice clouds during the ACB season, in which the peak activity was seen from $L_S 50^\circ$ to 115° (Lemmon et al. 2015).

Using the Surface Stereo Imager (SSI) on board the Phoenix Lander, Moores et al. (2010) observed a variety of high-latitude cloud types in the atmospheric movies captured throughout the mission (from $L_S = 102^\circ$ to 146°). Given the location of Green Valley at 68°N , and 233°E , the landing site of Phoenix, these observed clouds are not ACB clouds. Rather, they are more likely to be NPH clouds, although seen early in the season. Cirrus-like clouds were prevalent in the early morning and at late-night times, whereas denser and lower cumulus-like clouds were seen mid-sol, suggesting convection of nearly saturated air near the surface.

The Phoenix results were compared by Moores et al. (2015) with clouds observed by the Navigation Camera (NavCam) on board the Curiosity rover at Gale Crater, the rover’s landing location. The results showed that Gale crater is drier than Green Valley, and the variable optical depth of the cloud features was also considerably smaller at Gale. The diurnal and seasonal patterns seen at Gale Crater, located at latitude 5.4° South and longitude 137.9° East, were comparable with the ACB season. The peak cloud activities, determined by cloud opacity, were observed in the morning/afternoon and around the ACB period (Kloos et al. 2018). They have also been reported to leave a thermal signature at night on Gale’s surface (Cooper et al. 2021), again demonstrating the importance of the radiative impact of water-ice clouds on the lower atmosphere as well as on the surface.

Although we understand the larger cycle of clouds in the aphelion region, in this study, we focus on specifically analyzing the clouds seen at Jezero Crater, the landing site of the Mars2020 Rover Perseverance. Like Gale Crater, Jezero Crater is also located within the ACB cloud region at 77.5°E longitude, 18.4°N latitude. Therefore, we employed techniques that were previously used with Curiosity at Gale Crater by Moores et al. (2015) and Campbell et al. (2020), in addition to image-processing techniques to study the cloud structures and cloud occurrence in the first 600 sols of the mission. In this paper, we focus on movies and surveys collected using the NavCam instrument on board the rover to study Martian clouds at Jezero Crater.

In Section 2 we discuss the data set we acquired with the NavCam instrument on the Perseverance Rover, followed by a description of the methods in Section 3. Section 3 is split into four subsections starting with the preprocessing techniques we used to correct the NavCam images for camera geometry and viewing angle geometry and to highlight the mean-frame subtraction method we used to enhance the cloud features. The subsequent subsections show the various methods we used to

identify, detect, and characterize the cloud features observed at Jezero Crater. Section 3.1.2 contains our results and a discussion describing the statistical characteristics of the Mars clouds and the sizes of the cloud structures over Jezero. This section also contains the resolution and threshold dependence analysis for detecting cloud structures over different ranges. We finally present the conclusions of our results in Section 3.1.3.

2. Data Set: Cloud Surveys and Cloud Movies

NavCam is a mast-mounted stereo pair of engineering cameras that capture color images with a $96^\circ \times 73^\circ$ field of view at $0.33 \text{ mrad pixel}^{-1}$ resolution (Maki et al. 2020). The main purpose of NavCam is to survey the terrain for traverse planning, science target selection, robotic arm operation, and rover-enhanced navigation (ENav). Although initially designed as engineering cameras, the camera pair is radiometrically calibrated and thus can be used to carry out scientific investigations. These Mars2020 engineering cameras are similar to the engineering camera on the MER and Curiosity Rover with some major improvements. Unlike the previous rovers’ engineering cameras, which used black and white charge-coupled device (CCD) detectors, the NavCam on Perseverance is equipped with updated complementary metal-oxide semiconductor (CMOS) detectors that allow color-imaging capabilities. The Perseverance NavCam also has a wider field of view and finer pixel scale (mrad pixel^{-1}), allowing for more detail to be resolved over larger areas.

Both the left- and right-eye camera are mounted on the rover’s mast and are placed 16.5 inches (42 centimetres) apart. The NavCam uses a global-shutter CMOS sensor with a resolution of 5120×3840 pixels. Due to limitations in the camera electronics, images from the NavCam must be read out from the detector in data segments of 1280×960 pixels. At full resolution, each segmented readout accounts for one-sixteenth of the entire acquired image, but images may be downsampled by up to four times in each dimension (4×4 pixel binning) to obtain an image covering the entire extent of the detector in a single readout command.

The NavCam is used to collect two types of measurements for cloud study: cloud surveys, and cloud movies. Cloud surveys consist of five panoramic images covering the entire sky, including four images taken at $\sim 25^\circ$ elevation, $\sim 0^\circ$, 90° , 180° , 270° azimuth, where 0 degrees is defined as due North, and one zenith image taken at $\sim 79^\circ$ elevation, $\sim 96^\circ$ azimuth. These measurements are usually taken twice a week at different times of day. In contrast, cloud movies are designed to capture a single portion of the sky over a longer period to create a time lapse. These observations involve taking eight frames looking toward the horizon at 15 s intervals, producing a time-lapse movie containing cloud movements. Figure 1 shows cloud observations acquired in the first 600 sols. Cloud surveys are represented as blue stars, cloud movies as red dots, black circles indicate images where water-ice clouds were seen, and the gray rectangle covers the ACB season from $L_S 45^\circ$ to 140° (Clancy et al. 1996; Wolff et al. 1999; Tamppari et al. 2000, 2003).

The images and movies collected by NavCam can be found on the Planetary Data System (PDS). The fundamental data record (FDR) products, located within the calibrated data bundle, are formatted to include a geometric reconstruction of the full-size engineering camera image. This reconstruction

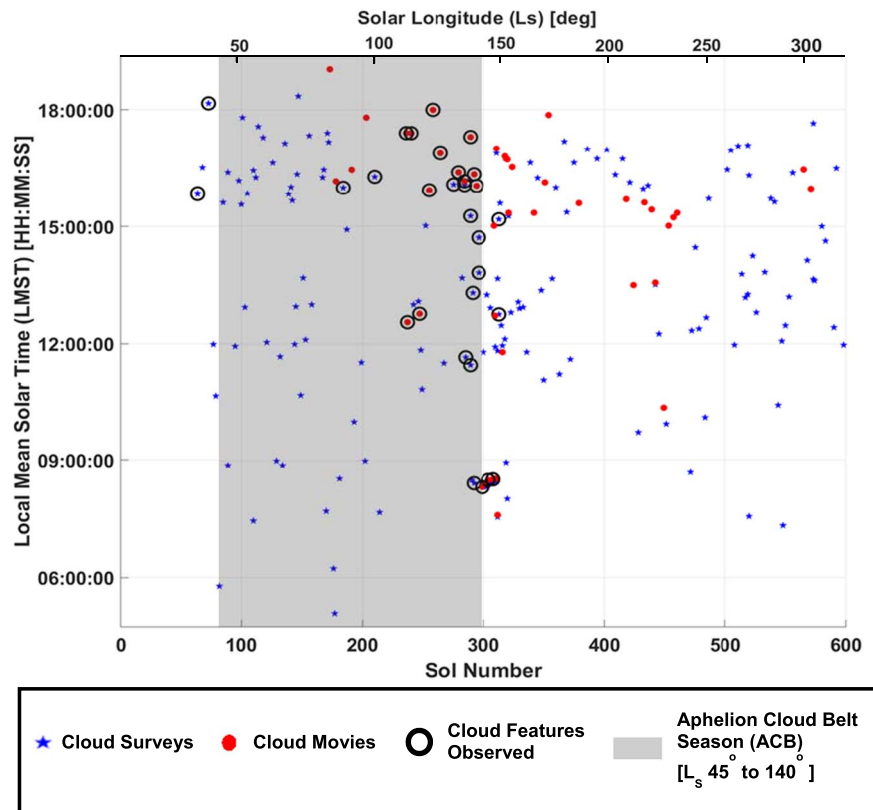


Figure 1. Distribution of NavCam cloud observations at various times of sol as a function of solar longitude, LS, and mission sol number. Red dots are cloud movies, blue stars are cloud surveys, and black circles are observations in which we have seen clouds. The gray box highlights the ACB season from $L_s \sim 45^\circ$ to $\sim 140^\circ$.

uses all detector readouts available for a specific acquisition. This additional reconstructed product is required due to the limitations of the maximum allowable readout size of 1280×960 pixels from the detector. The reduced data records (RDR) bundle is comprised of all images derived from the previously described bundles, including radiometrically corrected images, stereo correlation products, and products used for rover planning and analysis. The RDRs include radiance-corrected RAF (rad-corrected absolute radiance units—Float) and RAS (rad-corrected absolute radiance units—Scaled) products. RAF products have floating point values representing raw radiance values in units of $\text{W m}^{-2} \text{nm}^{-1} \text{sr}^{-1}$. For this study, FDR data were used as they are the cleanest products with the least noise and thus are best for studying cloud structures, while RAF products are better suited for investigating cloud or sky brightness.

3. Methods

In this section, we first highlight the preprocessing technique used on the NavCam cloud movies, which is called mean-frame subtraction, to emphasize the cloud features. We analyzed the processed movies visually to identify the presence of water-ice cloud features. The identified movies were then projected using the CAHVORE model and were analyzed further using image-processing techniques.

3.1. Preprocessing of NavCam Cloud Movies

3.1.1. Mean-frame Subtraction

The NavCam cloud movies were captured in red, green, and blue (RGB) color. To enhance the visibility of moving features,

the green channel was selected for further analysis, given its robustness. The frames underwent additional processing using the MFS technique. This method has been employed in previous studies (Moores et al. 2015; Campbell et al. 2020). In this technique, a mean frame was generated by summing the pixel intensities of all eight frames of each movie and dividing the total by eight. The resulting mean frame was then subtracted from each individual frame, highlighting the moving features. In Figure 2 (available as an animation in the HTML version), the NavCam cloud movie captured on sol 292, LMST 16:23 is presented on the left, and the MFS-processed movies are shown on the right. Figure 3 offers a comparison of raw FDR frames 1, 3, 6, and 8 with their corresponding MFS-processed counterparts. The distinct shape, movement, and seasonality of these features indicate that they are water-ice cloud features.

3.1.2. Dust versus Water-ice Clouds

All MFS-processed NavCam cloud movies were visually examined for cloud features. Out of the 46 cloud movies collected in the first 600 mission sols, 18 contained definitive cloud features that traverse frame to frame. To differentiate between dust and water-ice cloud features in the cloud movies, multiple co-authors independently reviewed the movies and identified instances of potential water-ice cloud features, based on insights gained from literature and previous missions. While some ambiguity may exist in classifying certain cloud features, previous works have suggested that water-ice clouds generally exhibit stronger and brighter features that retain their shape over time, while dust clouds diffuse more rapidly and appear less bright in MFS frames (Moores et al. 2010, 2015;

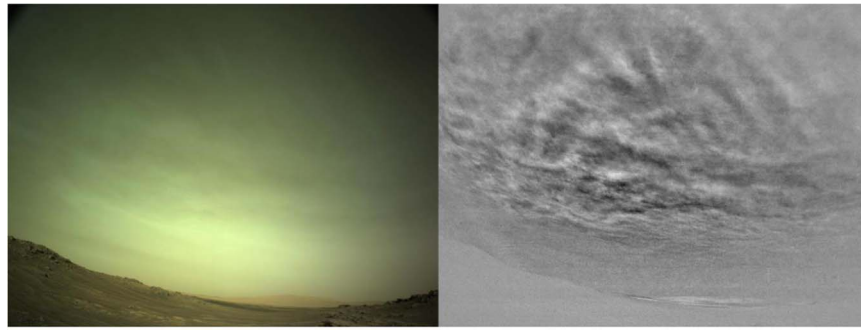


Figure 2. A still of frame 1 from the eight-frame animation available in the HTML version. The animation sequentially displays the raw NavCam cloud movie from sol 292 on the left and its corresponding MFS-processed frames on the right, displaying the cloud dynamics over the duration.

(An animation of this figure is available.)

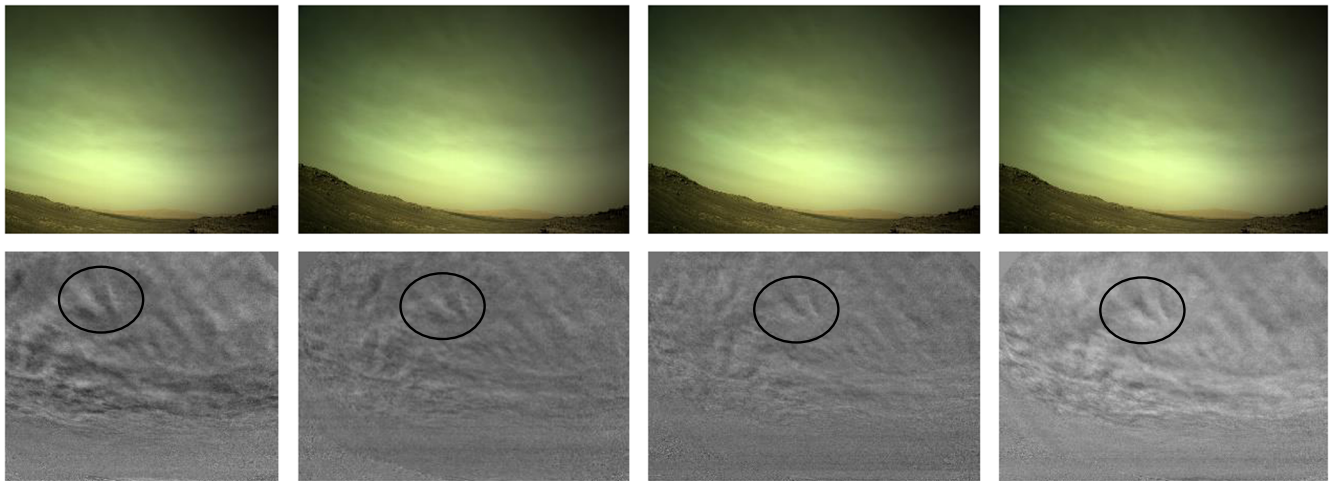


Figure 3. The top four images depict the raw FDR frames 1, 3, 6, and 8 from the NavCam cloud movie captured on sol 292 at LMST 16:23. By observing the prominent cloud features, for example, features enclosed within the black circles, it is noticeable that these clouds exhibit a general diagonally downward motion.

Campbell et al. 2020). Furthermore, surface-based dust activity, such as dust devils, are inherently linked to the ground, in contrast to water-ice clouds, which are seen unattached. Given this prior knowledge, cloud movies with notable water-ice cloud features were identified to be between sol 236, L_S 111.9° to sol 310, L_S 147.52°, and the strongest features are seen on sols 292 and 294, L_S 138°–139°. Figure 4 shows an example of a frame from sol 292 containing water-ice cloud features in the entire frame, and a frame from sol 319 containing dust cloud features toward the top right corner of the image.

Furthermore, we investigated the color capabilities of the NavCam to determine whether the blue and red channels could be suitable for differentiating between dust and water-ice clouds. However, the red and blue channels introduced chromatic noise into the MFS-processed frames, and artificial circular banding patterns were observed in the images that overshadowed the cloud features (see Appendix for more details). Therefore, the green channel was selected for the analysis, as it was deemed more suitable for this study.

3.1.3. Cloudiness Index

NavCam cloud movies with water-ice cloud features were visually analyzed and given an cloudiness index from 0 to 5. Here, 0 means that no clouds are seen in the processed movies, and 5 means that it was very cloudy (see Table 1). A similar

ranking scheme has previously been successfully used by Moores et al. (2015) to visually identify cloud features in MSL cloud movies. In this case, four of the co-authors independently evaluated these images, and an average index of cloudiness was noted for each cloud movie. This cloudiness index is then compared with the statistical and morphological parameters to examine how image-processing techniques compare to visual estimates of the cloud features.

3.1.4. Image Projection

The NavCam uses a fisheye lens to capture a wide field of view, which introduces distortions that require correction for a realistic and geometrically accurate representation of the sky. Additionally, the NavCam cloud movie frames were acquired from the ground, covering a substantial portion of the sky. It is crucial to note that these images also exhibit angle view bias, leading to variations in the perceived sizes of cloud structures. For example, a horizontal cloud structure covering area A on the horizon appears smaller in the image than a cloud structure of the same area A at the zenith. To address this view angle bias, we employed a projection technique by mapping the captured images onto a plane positioned above the rover at expected cloud heights. This approach facilitated accurate comparison of cloud sizes and shapes. By combining the correction for the fisheye-lens distortion and the mitigation of

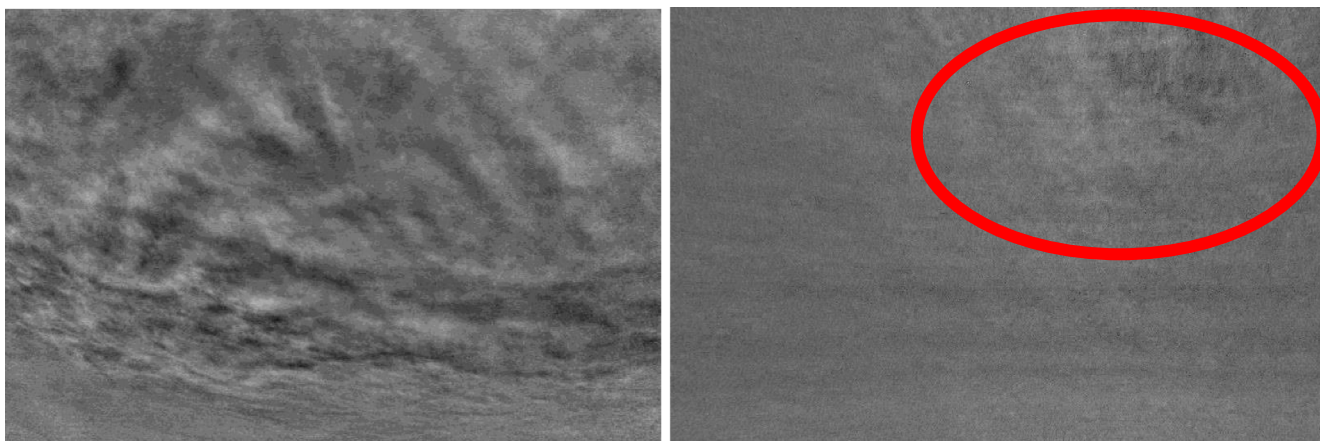


Figure 4. MFS-processed frame from sol 292 (left) containing water-ice cloud features and from sol 319 (right) containing dust cloud features toward the top right corner of the frame.

Table 1
Visual Estimates of the Cloudiness Index

Index	Description
0	No presence of clouds
1	The possible presence of clouds in at least 2 frames of the movie
2	Small parts of the sky covered in cloud structures in at least 4 frames
3	Medium parts of the sky covered in cloud structures seen in 6 or more frames
4	Large parts of the sky covered in cloud structures in all frames
5	Full sky covered in clouds in all frames

view angle bias, our method ensured reliable and geometrically accurate projections.

Our method involved three major stages: (1) initializing a grid of 3D points representing a plane in the sky, (2) transforming these 3D points into image-pixel coordinates using the CAHVORE camera model based on Gennery (2006) and Di & Li (2004), and (3) generating a resultant image by interpolating the original image at the transformed coordinates.

(1) Setup of the 3D Point Grid

We established a grid of 3D points representing a virtual plane positioned h km above the Mars2020 rover, where h represents the height of the plane. Based on vertical profiles of the water ice obtained with the Mars Climate Sounder (see Section 4.3.1) and twilight cloud heights observed using the Perseverance Radiation and Dust Sensor (RDS; Apestigue et al. 2022; Toledo et al. 2023), heights ranging from 30 to 50 km were selected. We assumed that all clouds exist within a single layer at the given cloud height, neglecting the curvature of the plane at the cloud base within the field of view. The grid covered east–west and north–south distances from -250 to $+250$ km. These grid limits ensured a comprehensive view of the Martian sky and served as a reference for projecting each part of the NavCam image onto the sky. We then rotated this plane using quaternions into rover frame to prepare for the next step.

(2) CAHVORE Camera Model

The CAHVORE camera model was selected for the projection due to its ability to accurately describe the geometric relation between the 3D world and the 2D image, while also

accounting for radial and tangential lens distortions. The CAHVORE model accounts for various factors; these parameters are in rover frame and can be found on the PDS. The \mathbf{C} vector denotes the camera position in world coordinates, while the \mathbf{A} , \mathbf{H} , and \mathbf{V} vectors describe the alignment and orientation of the image plane with respect to the camera. The \mathbf{O} vector defines the optical axis of the lens, and the \mathbf{R} and \mathbf{E} parameters account for radial and tangential lens distortion, respectively.

This model takes as input the CAHVORE parameters and the 3D coordinates in the world plane, in this case, from the defined plane, and maps them to 2D coordinates in the image plane taken by the camera, accounting for the orientation and position of the camera, as well as the characteristics of the fisheye lens. This allows it to map the view of the sky onto the image, creating a corrected projection that can be used for further analysis.

(3) Image Interpolation

Finally, the `interp2` function on MATLAB (MathWorks, Natick, MA) was used to interpolate the original image at the pixel coordinates computed by the CAHVORE model. This function uses a linear interpolation method that estimates the pixel values at the calculated coordinates based on the values of the surrounding pixels in the original image. The output of this interpolation is a new image that represents the view of the Martian sky projected onto the defined plane. We applied this interpolation to the MFS frames of the cloud movies, excluding the bottom ~ 200 pixel rows to remove the surface from the frames. The resulting image shows the correction for the fisheye lens and projection to a height above the surface; an example is shown in Figure 5 (animation available in the HTML version) for sol 292 at a height of 40 km.

3.2. Statistical Cloud Characteristics: Mean, Standard Deviation, and 2D Fourier Transforms

Visual examination to detect clouds in the NavCam movies is a useful start; however, in terrestrial cloud research, this has been proven to be inconsistent and subjective (Hoyt 1978). Therefore, this has led to the use of digital image-processing techniques for detecting and characterizing Earth clouds. In this study, we examined the use of some of these Earth-tested digital image-processing techniques to detect and characterize Mars clouds. For all analyses presented here, linearized FDR products were used that were subsequently normalized and

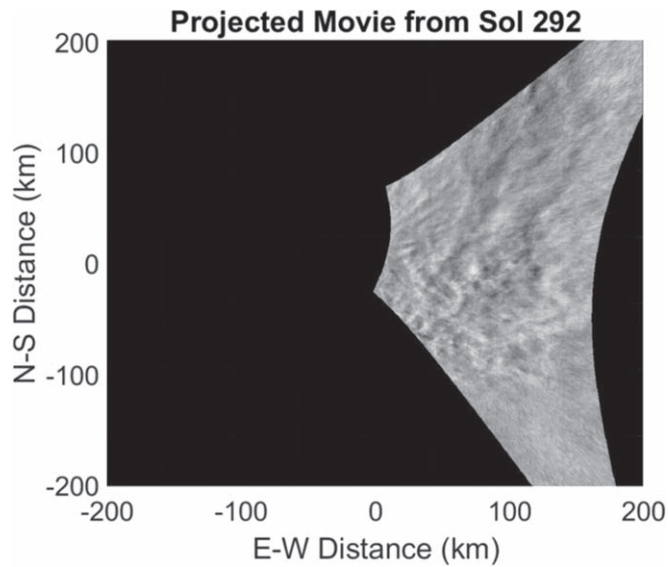


Figure 5. Frame 1 from sol 292 projected at a height of 40 km. (An animation of this figure is available.)

preprocessed using the MFS technique. Statistical parameters such as image mean, standard deviation, fractional sky cover, and peak power ratio were used to first identify cloud movies with cloud features and to further differentiate between dust clouds and water-ice cloud features. Subsequently, 2D Fourier transforms were used to characterize the cloud features further by finding the sizes of the structures. These techniques have previously been used successfully by, e.g., Calbó & Sabburg (2008), to characterize as well as classify terrestrial clouds in cloud recognition and cloud classification algorithms. Computing cloud classification algorithms for Mars clouds is beyond the scope of this study, but the parameters highlighted here can be used to create such an algorithm. Furthermore, these parameters allow for a comparison of processed cloud movies in the first cloudy season, and in the future, they will allow for quantitative comparisons across many cloudy seasons at Jezero Crater as more data are collected.

3.2.1. Mean and Standard Deviation

All the processed cloud movie frames were normalized grayscale images, such that the pixels are defined by one value. Hence, the information can also be presented as intensity histograms, in which each peak represents the number of pixels at that given intensity value (e.g., Calbó & Sabburg 2008).

The mean, \bar{x} , i.e., the average intensity value on an intensity histogram, was calculated with the following equation:

$$\bar{x} = \frac{1}{N} \sum_{i=1}^N x_i, \quad (1)$$

where N is the total number of pixels, and x_i is the intensity of the i th pixel. The standard deviation, STD , was calculated for each frame using

$$STD = \sqrt{\frac{\sum_{i=1}^N (x_i - \bar{x})^2}{N}}. \quad (2)$$

The image mean and STD parameters were used to identify NavCam cloud movies containing water-ice cloud features as well as to compare and characterize the variability of cloud features between different sets of processed cloud movies.

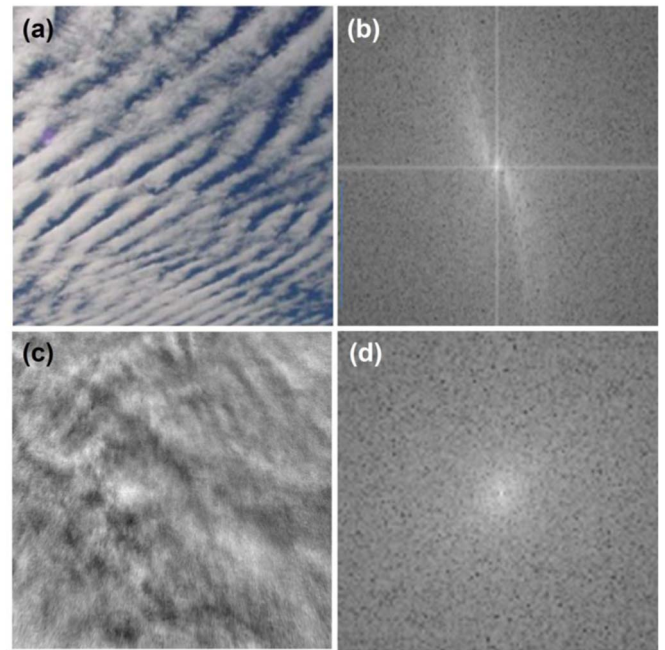


Figure 6. (a) Image of Earth clouds (credit: Author's own photograph, 2021). (b) Corresponding 2D FFT of Earth clouds, and (c) NavCam image of clouds from sol 292 (d) with the corresponding 2D FFT of Mars clouds.

These movies were compared with the visually determined cloudiness index from Section 3.1.3 to investigate how well these parameters perform in detecting Mars-cloud features.

3.2.2. Fourier Transforms

The statistical parameters highlighted above are useful in image characterization, but they lack information in determining cloud patterns. To characterize these patterns, we used 2D Fourier transforms that were previously used by Calbó & Sabburg (2008), Mohan et al. (1988), and Moores et al. (2015) to study terrestrial as well as Mars clouds. Analysis through Fourier transforms also ensures that the observed and characterized cloud features are not an artifact of the human mind, but are patterns that can be quantified using advanced digital image-processing techniques.

Fourier analysis is a versatile tool that is used in many signal- and image-processing techniques to characterize patterns. Here, we used it to transform an image from the spatial domain to the frequency domain while retaining information concerning patterns in clouds. The projected frames are trapezoid-shaped images (see Figure 5) instead of the ideal square shape required for the 2D FFT analysis. Thus, we adopted a strategy of selectively cropping a square region of interest from each projected frame and performing the 2D FFT analysis on these regions using a 2D FFT routine in MATLAB. The real part of the 2D FFT was then shifted to place the lowest frequencies in the center of the plot and the highest frequencies toward the edges. Figure 6 shows the Fourier transform of Earth clouds compared to Martian water-ice clouds observed by the NavCam instrument and their respective Fourier transforms. A strong diagonal pattern is observed in panel (a), which is reflected in the 2D FFT of the image shown in panel (b). Similarly, with Mars clouds, the 2D FFT of the image in panel (c) also shows a slightly diagonal and smaller feature in the center of panel (d) that corresponds to the

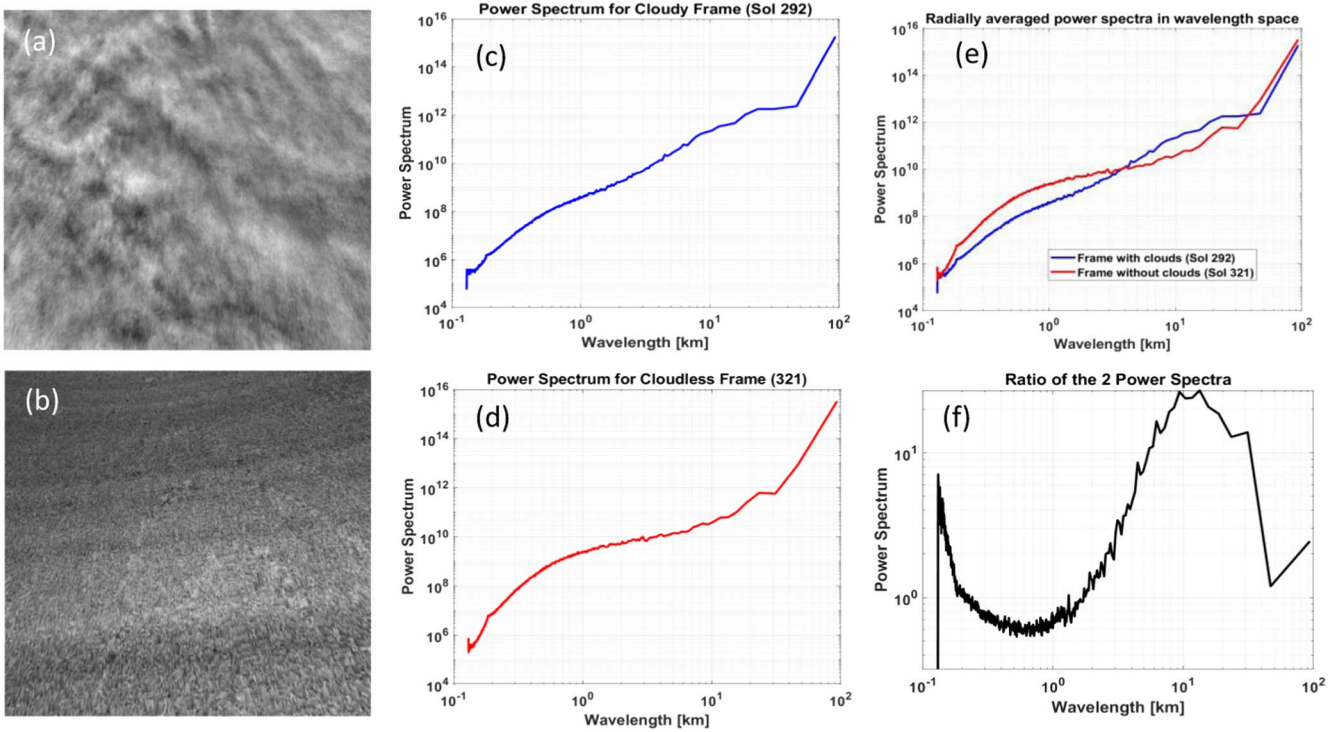


Figure 7. Panel (a) MFS-processed and projected frame at $h = 40$ km from sol 292 containing cloud features, and (b) MFS-processed frame from sol 321 containing no cloud features (noisy frame). Panels (c) and (d) are their respective radially averaged power spectra. Panel (e) shows the overlaid power spectra, and panel (f) shows the ratio of the two spectra, revealing where in the wavelength space the cloud features lie.

structures seen in Mars clouds, but on a smaller scale. It is worth noting that the 2D FFT representation of Mars clouds appears fainter due to their lower optical depth and subtler characteristics when compared to some terrestrial clouds.

3.2.3. Power Spectra of the Cloud Features

The 2D Fourier transform is then converted into a radially averaged 1D power spectrum to plot the power distribution over the frequency (and wavelength) range. The radially averaged 1D power spectrum is a direction-independent mean spectrum computed by averaging the power density at increasing concentric circles, starting from the center (lowest frequencies, highest wavelengths). Because the lowest frequencies with the highest power are in the center of the shifted 2D FFT image, the 1D power spectrum has a generally decreasing slope as frequency increases (i.e., wavelength decreases).

It is important to note that the maximum resolvable frequency in this analysis is determined by the Nyquist frequency, calculated as $1/(2 \times \text{resolution})$, with the resolution of the projected images being 100 m pixel^{-1} . This corresponds to a minimum resolvable wavelength of 200 m. The Nyquist frequency serves as an upper boundary for the range of frequencies that can be accurately represented in the sampled data. Frequencies above this are susceptible to sampling errors and are therefore disregarded in the analysis.

The 1D radially averaged power spectrum of an MFS frame containing cloud features was compared with the 1D radially averaged power spectrum of an MFS frame containing no cloud features and mainly noise. In Figure 7 the radially averaged power spectra of MFS projected frames from sol 292, panel (a), and sol 321, panel (b), are shown in panels (c) and (d), respectively. The individual power spectrum of the two MFS-

processed frames are overlaid and shown in panel (e), and panel (f) shows the ratio of the two spectra in wavelength space.

By taking the ratio of the two power spectra, we first determined where the cloud patterns are present in frequency space. Then, by assuming a range of heights between 30 and 50 km, we computed the sizes of these cloud structures. To avoid the angle view bias, all frames were first projected to cloud layers at five heights ranging from 30 to 50 km. Subsequently, their respective 1D power ratios were computed, and the wavelength, λ_{struct} , corresponding to their peak power ratio (PPR) was noted at all different heights. Because each cloud movie contained eight frames, we took the mean and standard deviation of the PPR and λ_{struct} of all eight frames. The mean values were noted as the estimated wavelength, i.e., the size of the cloud feature, for height, h , and the standard deviation served as the error bar.

In this study, a nominal cloud-free frame from sol 321 served as the reference for all PPRs and λ_{struct} values. We evaluated other cloudless frames from different sols and a synthetic noise-only image for comparison, finding that both options produced results that were consistent with those obtained using the sol 321 frame.

3.3. Image Segmentation: Thresholding, Fractional Sky Cover, and Resolution-dependent Cloud Structure Detection

3.3.1. Thresholding

The 2D FFT method highlighted in Section 3.1.1 is successful in determining the sizes of the Mars-cloud structures. However, to detect these structures in the frame itself, the thresholding technique in image segmentation is often used in terrestrial cloud research (e.g., Calbó & Sabburg 2008; Li et al. 2011). Here, we examined whether Mars-cloud structures can be detected using

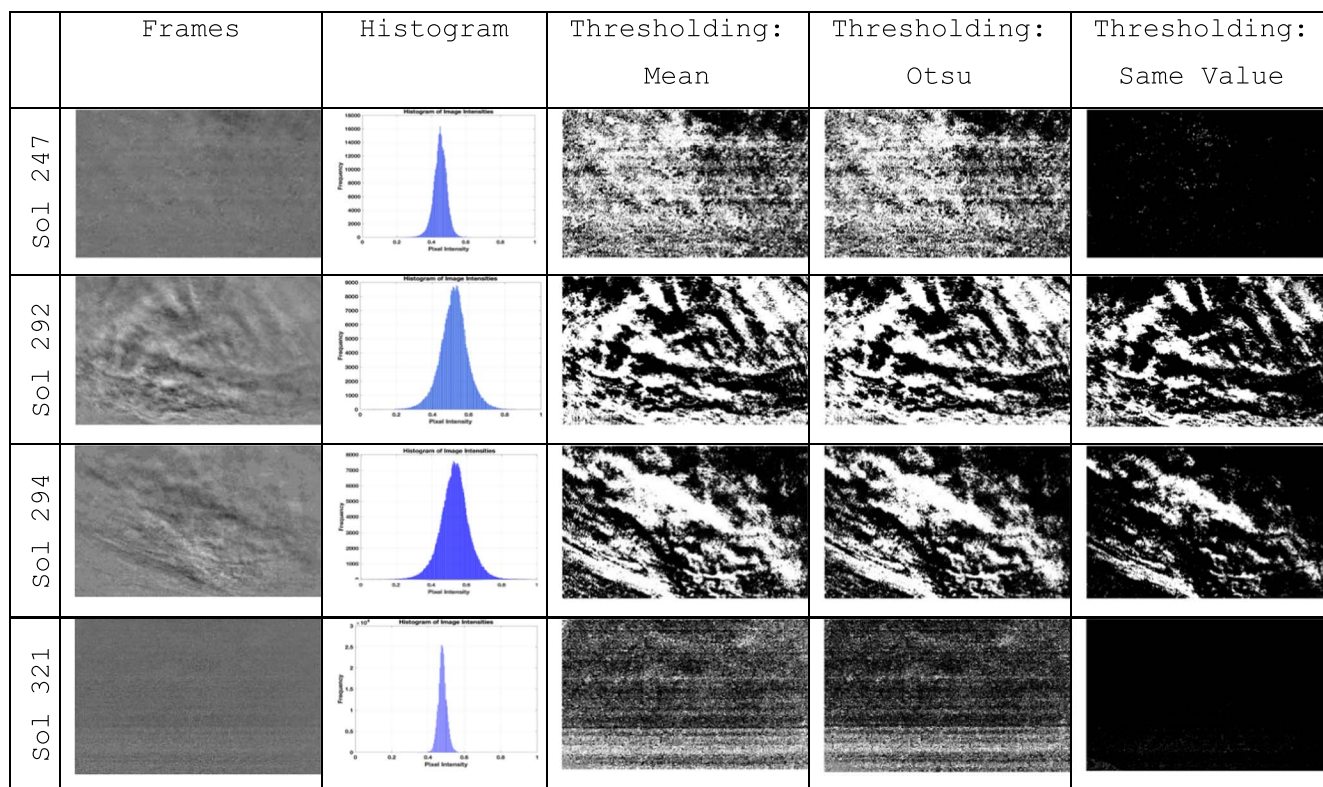


Figure 8. Mean frame subtracted frame from sol 247, 292, 294 and 321, their corresponding histograms followed by three sets of binary images using three different thresholding techniques: mean thresholding, Otsu thresholding, and same-value thresholding using 0.55. Unprojected frames are used for showcasing as they are visually better suited.

similar thresholding techniques by segmenting the pixels into a “foreground” or a “background” category using a threshold. The foreground, in this case, are water-ice cloud features, and the background are the noncloud feature pixels. There may be water-ice present in the part of the sky labeled “background,” but these pixels do not make up the cloud structures we see in the processed cloud movies.

Dust cloud features can also be present in the image. Because they are more uniform and do not vary strongly in optical depth, these features do not appear bright in an MFS-processed frame, as shown in Figure 4. They are also labeled “background” when thresholds are kept high as they have lower intensity values compared to water-ice cloud features.

To segment between a foreground pixel and a background pixel, three thresholding methods were investigated: mean thresholding, grayscale thresholding, and same-value thresholding. All foreground pixels were given the value of 1, and all background pixels were given the value of 0, creating a binary image of the NavCam frames.

The mean thresholding method involved labeling all pixels with intensities above the mean intensity found using Equation (1) as a foreground pixel and below as a background pixel. The mean value for thresholding is generally used as a first-guess threshold and works best for real-world images.

The grayscale thresholding consisted of taking the Otsu thresholding, a popular technique for performing automatic image thresholding. This method iterated through all possible threshold values and chose one that minimizes the sum of the foreground and background variance (Otsu 1979). Although the Otsu technique works best for images with bimodal

intensity peaks, it has been successfully used previously to distinguish terrestrial cloud features in sky images by Xiang (2018) and Yang et al. (2012).

The same-value thresholding method makes use of the same value to threshold all cloud movie frames. The MFS processing, highlighted in Section 3.1, involves taking the difference in intensity between a given frame and the mean frame. Therefore, pixels with a higher intensity difference contain water-ice cloud structures. The MFS processing also allows for a comparison between different sets of cloud movies from different times of the season and sol. Several thresholds were tested for this method, and 0.55, i.e., 55% of the image intensity histogram, was selected as it performed best in distinguishing cloud features in the selected cloud movies.

Figure 8 shows four frames from sols 247, 292, 294, and 321 and their corresponding histograms. Frames with water-ice cloud features contain larger variations in pixel values and therefore have wider histograms. The three different thresholds were used to compute binary images of the frame. Sol 247 shows dust features and no water-ice cloud features, both sol 292 and 294 contain water-ice cloud features in two orientations, and sol 321 contains no dust or cloud features. In all frames, both the mean and Otsu thresholding picked up noise along with cloud features as foreground. Specifically, they were less effective in segmenting out the water-ice cloud features. The same-value thresholding successfully isolated the bright water-ice cloud features from the frames as seen in the frames from sol 292 and sol 294. With these examples, we show that image thresholding can be used as a technique to detect Mars-cloud features. In the next section, we highlight how we used it further to characterize Mars clouds.

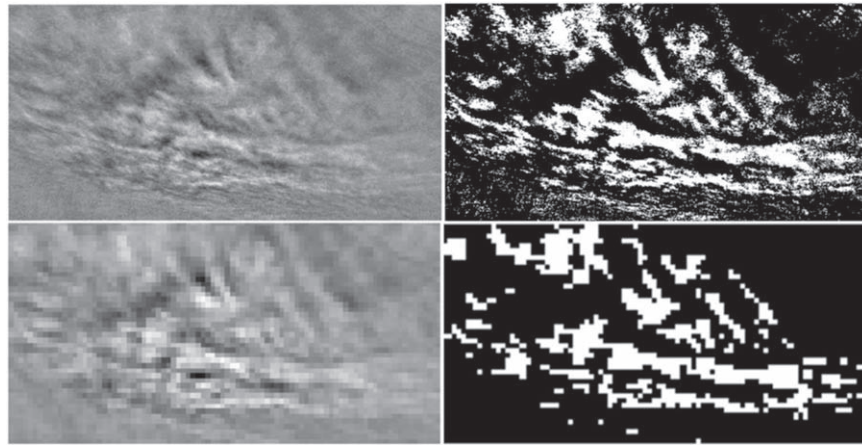


Figure 9. Functional box-counting method used to determine the resolution dependence of cloud feature fraction calculations. The top is the original image with $L = 0.1 \text{ km pixel}^{-1}$, and the bottom is degraded to $L = 0.8 \text{ km pixel}^{-1}$. Unprojected images are used here for visualization purposes only.

3.3.2. Fractional Sky Cover

After the frame has been segmented into foreground (cloud feature) and background (noncloud feature) pixels using the same-value thresholding method, highlighted in Section 3.3.2, the fractional sky cover (FSC), a measure for cloud fraction (Calbó & Sabburg 2008), of a projected and MFS-processed frame was calculated using

$$\text{Fractional Sky Cover, FSC} = \frac{N_f}{N}, \quad (3)$$

where FSC is the ratio of pixels in the image that corresponds to water-ice cloud features, N_f is the number of pixels labeled foreground pixels, and N is the total number of pixels in the frame. This parameter was used to identify the peak time at which we saw most water-ice cloud features in the sky at Jezero Crater in the first 600 sols.

3.3.3. Resolution Dependence of the Fractional Sky Cover

Ideally, FSC, i.e., the ratio of the image covered in cloud structures, can be used to determine the cloud cover, i.e., the ratio of the sky that is covered in clouds. However, detecting all cloud structures through the thresholding method highly depends on the resolution of the image as well as on the chosen threshold, as shown by Lovejoy et al. (1987), Gabriel et al. (1988), and Li et al. (2011). There could be cloud structures down to much smaller or larger scales that are not resolved at this fixed resolution. Here, we investigated how FSC varies with different resolutions and thresholds. First, this allowed us to determine the level of resolution needed for a camera to successfully image and detect Mars-cloud structures using the thresholding method. Second, with this, we investigated how FSC changes over decreasing resolutions, and we thus examined the self-similarity of the Mars clouds.

In 1975, Benoît Mandelbrot introduced the concept of fractals to describe patterns that are self-similar and infinitely complex. He also proposed the term “fractal dimension,” a noninteger value that can be used as a measure of the complexity of these fractal patterns (Mandelbrot & Wheeler 1983). Lovejoy (1982) proved that Earth clouds exhibit self-similarity across scales ranging from 1 to 1000 km and are fractals. Much like Earth, Mars clouds were shown to be fractals by Henderson-Sellers et al. (1986) using Viking imagery, and they exhibit a fractal dimension of 1.6. It was

subsequently realized that clouds are turbulent fields for which a single power law, i.e., the fractal dimension, was not enough to characterize the complexity, rather multiple dimensions would be required to characterize the clouds. Lovejoy et al. (1987) and Gabriel et al. (1988) demonstrated the multifractal characteristics of Earth clouds using the functional box-counting method. They showed that at different radiances, i.e., thresholds, T , the scaling was followed but the power laws were different for each T , thus proving that Earth clouds are multifractal—a combination of fractals over various thresholds. More recent work has also shown that not only frequency, but even the probability distributions of cloud properties can change their shape with image resolution (de la Torre Juarez et al. 2011).

We adopted the same functional box-counting method as highlighted in Gabriel et al. (1988) and Lovejoy et al. (1987) to investigate the resolution dependence on detecting cloud structures as a function of brightness thresholds. The image resolution was decreased in steps of two from 0.1 to 12.8 km pixel^{-1} in projected images. This was achieved by using bilinear interpolation, where the pixel value in the reduced image is computed by averaging the values of the corresponding 2×2 block of pixels in the original image. Figure 9 shows an example of Mars-cloud structures at two resolutions. To determine the scaling law, we first computed the resolution-independent term, $N(L)$,

$$N(L) = \frac{\text{Number of Pixels, } T' > T}{N}. \quad (4)$$

The $N(L)$, similar to FSC, is calculated at different L resolution scales and for a range of thresholds T . $N(L)$ was plotted as a function of L on a log–log graph, and the scaling power law was found by fitting a straight line to the points. We investigated how this varied over different resolutions and thresholds to determine the multifractal nature of Mars clouds.

4. Results and Discussion

4.1. Cloud Characteristics

A list of cloud movies from sol 236 to 310, L_S 111.9 to 146.5, along with a summary of their statistical characteristics and the visually determined cloudiness index is shown in Table 2. The following cloud movies, highlighted in blue, sols 240, 264, 284, 289, 292, and 294, have a cloudiness index of 4 and higher, meaning that they are visually very cloudy. They

Table 2
Summary of the Statistical Characteristics of Cloud Movies from sol 236 to sol 310

Sol	Solar Longitude LS	LMST	Standard Deviation (averaged)	Fractional Sky Cover	Peak Power Ratio	Cloudiness Index (Averaged)
236	111.93°	17:26	7.95	0.04	8.30	3.80
237	112.39°	12:34	8.17	0.02	10.07	3.60
240	113.77°	17:27	9.14	0.13	7.80	4.10
247	117.01°	12:47	5.11	0.04	6.20	2.30
255	120.74°	15:57	5.12	0.00	5.40	1.90
258	122.15°	18:02	5.52	0.00	9.40	2.50
264	124.98°	16:54	12.52	0.09	13.50	4.20
279	132.16°	16:26	9.01	0.00	9.32	1.40
284	134.59°	16:10	7.82	0.08	12.30	4.30
289	137.04°	17:20	14.26	0.40	12.31	5.00
292	138.52°	16:23	15.49	0.37	26.64	4.99
294	139.50°	16:00	12.82	0.48	19.36	4.90
299	141.99°	08:29	7.13	0.10	11.90	3.10
303	143.99°	13:15	7.75	0.00	9.39	2.80
304	144.49°	08:25	7.59	0.00	9.39	3.40
308	146.51°	08:30	5.86	0.00	5.53	0.00
309	147.02°	15:01	6.66	0.00	8.70	0.00
310	147.52°	12:43	6.48	0.00	7.56	0.00

are also movies with a higher standard deviation value, fractional sky cover, and a higher peak power ratio.

4.1.1. Mean and Standard Deviation

The image mean and standard deviation were first to be examined. In the 18 MFS-processed cloud movies, the image mean did not show a strong trend that could be used to differentiate between a cloudy and a noncloudy movie.

The standard deviation, however, showed a stronger relation with the visual determined cloudiness index than the mean. Higher standard deviation values reflect higher contrast in the MFS frames, consistent with the presence of cloud structures. The standard deviation values of all eight frames were averaged, and these values are noted in Table 2. The values range from 5.11 to 15.49 at sol 247 and sol 292, respectively. The overall low standard deviations are because of (1) the low optical depths of Mars clouds, and (2) the MFS processing, which subtracts all strong and contrasting features that are constant from one frame to the next, i.e., the surface. Furthermore, the presence of stronger features with higher contrasts within the frame is suggestive of water-ice clouds because dust clouds have less definitive structures, as shown in Figure 4.

These results indicate that using standard deviation as a parameter can be successful in identifying cloud movies with cloud structures, and this can be used in the future, for example, when creating a Mars-cloud detection or classifier algorithm. Because we had a small number of movies with water-ice cloud structures, each frame per movie was used as an independent measure, and the standard deviation for

each frame was computed separately. This increased the data set, but it is still limited when it comes to differentiating between different types of clouds. By comparing the standard deviation values with the visual scale, we were able to conclude that frames with a standard deviation of 9 and higher contained water-ice cloud features and frames with a standard deviation of 5 did not, as shown in Figure 10. The middle range is unclear, and those frames would require additional investigation. The standard deviation values were also used to determine the cloudy period. Figure 11 shows the values of standard deviation against sol number, and the overall timeframe when water-ice cloud features were seen in the NavCam cloud movies is shown in the orange box from sol 236 to sol 310. The peak cloudy period with the highest standard deviation values was seen between sol 284 and 294. This is shown in a gray box.

4.1.2. Fractional Sky Cover and Peak Power Ratio

The FSC measurements using the same-value thresholding method described in Section 3.3.2 as well as the PPR highlighted in section 3.2 are two additional parameters that were successful in identifying images with cloud features. As shown in panel (a) of Figure 12, cloud movies with a higher cloudiness index were seen to have a higher fractional sky cover, with the highest fractional coverage of 0.48 measured on sol 294. A higher FSC value indicates that a larger area of the image is covered in water-ice cloud structures. Using FSC, cloud movies between sol 284 and 294 were found to contain the largest number of water-ice cloud features in the sky, which

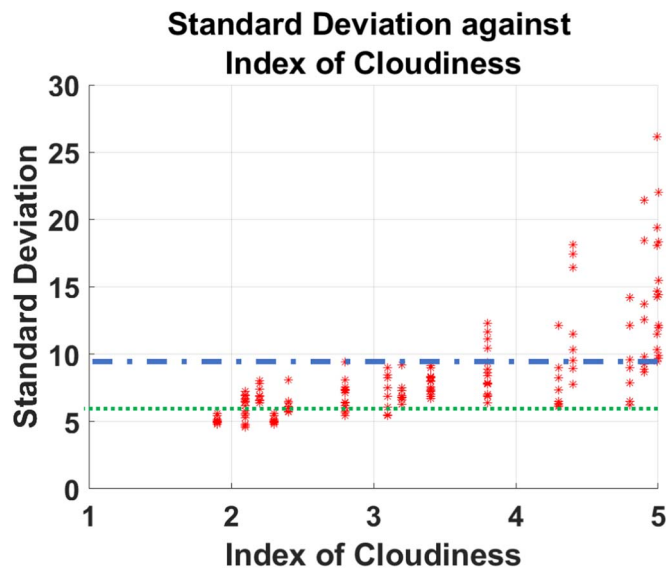


Figure 10. Graph of the standard deviation vs. cloudiness index. The frames with standard deviations above 9, the dashed blue line, contain water-ice cloud features, and standard deviations below 5, dotted green line, do not contain any water-ice cloud features. Cloud frames with a standard deviation between 5 and 9 would require further investigation.

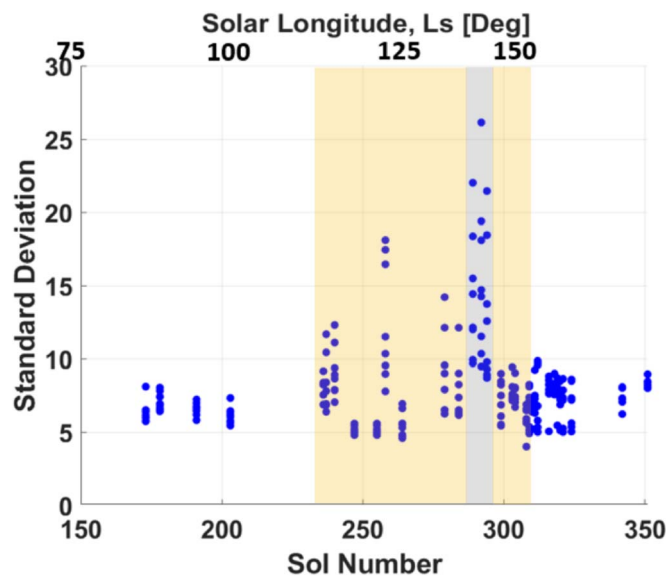


Figure 11. Standard deviation of each frame for cloud movies between sol 150 and 300 plotted against sol number and L_s . The orange box between sol 236, L_s 111.93°, to sol 310, L_s 147.52°, encompasses the overall time period when water-ice clouds were observed, with the peak period seen between sol 284, L_s 134.59°, to sol 294, L_s 139.5°.

also matched the peak period highlighted in Figure 11 (gray box). The seasonal implications are discussed below.

Similarly, the PPR, the maximum difference in the 1D power spectra (see Section 3.1.1) between an MFS-processed cloudy frame and a noisy frame, showed the same trend. Cloud movies with a higher cloudiness index also corresponded to a higher PPR, as shown in panel (b) of Figure 12. Furthermore, panel (c) of Figure 12 shows the FSC against PPR in log-log scale, where cloud images with higher FSC, i.e., frames containing more area covered in cloud features, also demonstrated a higher maximum power ratio. This graph illustrates that the cloud features detected via the same-value thresholding method are

likely the same cloud structures that are identified with the 2D FFT method. This further verifies that both methods are successful not only in identifying movies with cloud structures, but also in detecting the cloud structures themselves.

4.1.3. 2D FFT: Size of the Cloud Structures

A total of five cloud movies were selected for further examination because visually, these cloud movies contained strong cloud features that would be successful in calculating the structure size. All frames were projected to five cloud heights ranging from 30 to 50 km; their respective PPRs and corresponding wavelengths were computed.

As the cloud features have soft edges and visually varying brightness, it was initially thought that the 2D FFT algorithm was detecting cloud spacings, i.e., the darker areas in the projected image, because they are more visible. However, the same methods were repeated for a set of binary images that were segmented using the same-value thresholding technique. This meant that the images were now uniform in cloud brightness, such that all cloud features above a given threshold were labeled 1 and all background pixels below the threshold were 0. The results showed a marginally lower PPR but the same corresponding wavelength, showing that the 2D FFT method indeed detected cloud structures in the grayscale images.

The cloud structure sizes of the five cloud movies are highlighted in Table 3. For example, at $H = 30$ km, these structures ranged from 2.9 to 9.44 km. Using similar methods and instrumentation, Moores et al. (2015) examined cloud feature spacings because the cloud structures themselves were difficult to detect in the data set from the Curiosity Rover. The spacing sizes in Moores et al. (2015) range from 2.2° to 6.5°, with an average spacing size of 3.8°, which translates into 2.0 km at 30 km cloud height and 3.2 km at 50 km cloud height. The cloud structures we saw at Jezero Crater are visually comparable to the structures seen at Gale Crater. The difference in the sizes of the structures could be due to latitudinal differences or topographical differences between the two landing sites.

These size calculations were carried out over a small data set because only a limited number of cloud movies were collected in the first year of the mission. However, with a larger data set, this method can be used to differentiate between different sizes of cloud structures, and thus, to potentially classify different types of Mars clouds.

4.2. Image Segmentation: Resolution and Threshold Dependence Analysis

The thresholding technique is an effective image-segmentation method for detecting cloud features in an MFS-processed NavCam frame. Using the box-counting method, highlighted in Section 3.3.3, we determined the resolution dependence on being able to segment these cloud structures at different thresholds. The resolution-independent term, $N(L)$, was plotted as a function of resolution, given as the pixel length L , and thresholds, T . Figure 13 shows the results from sol 292, projected on a plane at 40 km. The frame resolution was degraded by increasing the unit pixel length, L , from 0.1 km per pixel to 12.8 km per pixel in steps of 2.

All pixel values in an MFS-processed frame were normalized to fit between 0 and 1 such that a higher threshold, T , represents the brighter regions of a frame. The overall

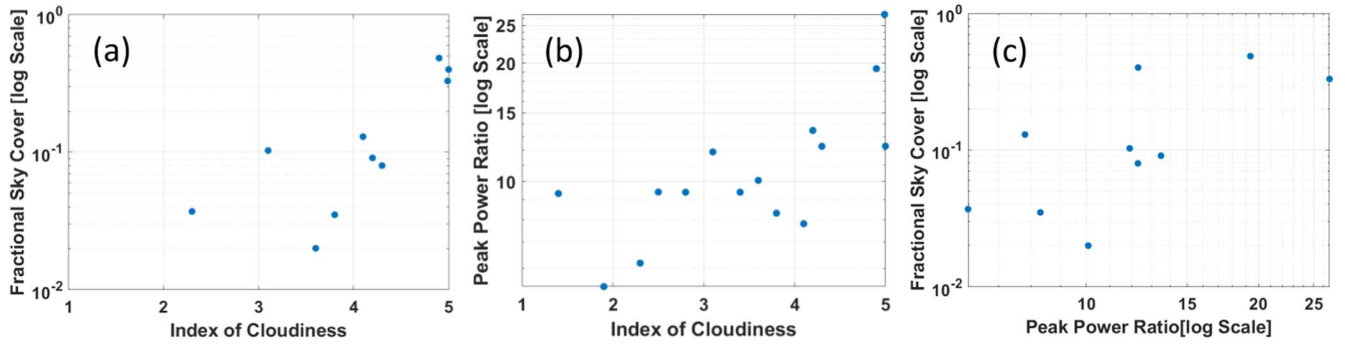


Figure 12. (a) Fractional sky cover in log scale against the cloudiness index, (b) PPR against the cloudiness index, and (c) FSC against PPR in log–log space.

Table 3

Summary of the Cloud Structure Sizes at 5 Heights, h , and for 5 Cloud Movies between sol 264 to sol 294

Sol	264	284	289	292	294
Solar Longitude, LS	125.0°	134.6°	137°	138.5°	139.5°
At $h = 30$ km, in [km]	6.2	2.91	4.23	9.44	2.9
Error in [km]	0.8	0.4	0.3	0.5	0.3
At $h = 35$ km, in [km]	7.39	3.48	5.08	10.94	3.48
Error in [km]	0.9	0.5	0.6	0.7	0.4
At $h = 40$ km, in [km]	8.06	4.59	6.24	12.06	4.59
Error in [km]	1.1	0.7	0.8	0.9	0.5
At $h = 45$ km, in [km]	9.53	6.61	8.83	14.38	6.61
Error in [km]	1.5	0.9	1.0	1.2	0.5
At $h = 50$ km, in [km]	10.34	8.66	10.18	15.25	8.66
Error in [km]	1.9	1.2	1.3	1.5	0.9

downward slopes suggest $N(L)$, the ratio of pixels representing the cloud structures above a given threshold, T , and total number of pixels in a frame, decreases as L , the resolution, decreases. As the resolution is degraded, the soft edges of the cloud structures become washed out in the binning process, resulting in a decrease in the overall $N(L)$ ratio (see Figure 9).

The straightness of the lines shows that scaling is followed, showing the fractal nature of Mars clouds. A total of 11 thresholds were chosen between 0.44 and 0.66, where 0.44 was selected as the lowest threshold to avoid noise being segmented as signal, and 0.66 was the highest to ensure there was enough signal to be processed during segmentation.

In Figure 13, at the specific thresholds examined, the scaling holds for ranges at least between $L = 0.1$ km to $L = 1.6$ km. Two conclusions can be drawn about these water-ice cloud structures examined using the box-counting method: (1) the cloud structures are detectable in the minimum resolution range from $L = 0.1$ km to $L = 1.6$ km using the thresholding method, and (2) they exhibit multifractality as the power laws are different for each threshold, T .

With the first conclusion, we are able to deduce the resolution needed for camera systems on landers/rovers to detect these cloud structures using the thresholding method. The cloud structures detected here were only examined for clouds seen at Jezero Crater and assumed to be between heights of 30–50 km. If one is interested in detecting these specific types of cloud structures, the camera system will require a resolution of at least 1.6 km pixels⁻¹ for clouds between 30 and 50 km. This corresponds to a camera resolution of 0.032

radians pixel⁻¹ assuming a maximum height of 50 km. It is also worth noting that this is specific to the thresholding method used to detect cloud structures, and with different detection methods, cloud structures may be detectable at other resolution ranges.

With the second conclusion, we show the multifractal nature of clouds, as was done with terrestrial clouds by Lovejoy et al. (1987) and Gabriel et al. (1988). The power laws, i.e., the slope of the lines, computed using linear regression, shown in the legend in Figure 13, decrease as the thresholds are increased in increments of 0.02. To illustrate that these slopes are significantly different from each other, we calculated the 95% confidence intervals for each slope. These intervals indicate a range within which we are confident at 95% that the true slope lies. First, the standard deviations of the slopes were computed for each threshold, and the standard error was calculated by dividing the standard deviation by the square root of the number of observations. A multiplication by 1.96, corresponding to a 95% confidence level, produced the interval width. Figure 14 presents the slopes along with their respective 95% confidence intervals, displayed as error bars, for the different thresholds. This figure reveals that the slopes indeed differ across thresholds, and that for higher thresholds, the confidence intervals do not overlap, indicating significant differences.

For lower thresholds between 0.44 and 0.54, a single power law can be used to characterize the self-similarity of the cloud structures. However, for thresholds higher than 0.54, the power laws fall outside of the intervals of other slopes and are significantly different. This shows the multifractal nature of Mars-cloud structures where multiple power laws are needed to characterize the cloud fields over different thresholds. Cloud fields are complex, turbulent fields that interact with other atmospheric fields down to much smaller scales in the millimeter range. The inhomogeneities of the various atmospheric fields introduce a range of strong scale dependences that appear in the power laws for different thresholds at different resolution ranges. This creates a complex system exhibiting a multifractal nature that is governed by other turbulent fields.

Another aspect to note is that the power laws, i.e., the slopes of the lines in Figure 14, range from -0.04 to -0.23 . Although these are significantly different, the difference is rather small compared to the terrestrial cases highlighted in Gabriel et al. (1988). This is because the threshold variations available in this data set are limited because the Mars clouds are optically thin and subject to the MFS processing. In Gabriel et al. (1988), the threshold ratio of each threshold, T , was 4.7, allowing for larger variations in the slopes.

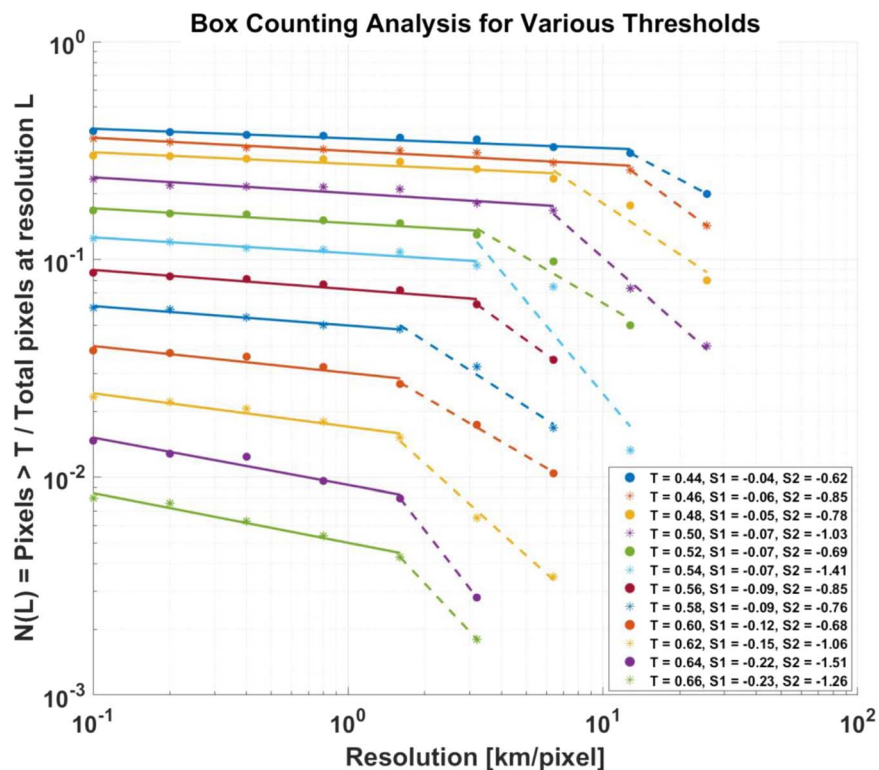


Figure 13. $N(L)$ as a function of resolution and threshold, portraying the multifractality of Mars clouds. The legend indicates the threshold (T) and the fitted slopes ($S1$ and $S2$). $S1$ is represented by a solid line and $S2$ by a dotted line, highlighting the break in the slopes.

For a threshold (T) of 0.44, the scaling power law is applicable for ranges from 0.1 to 12.8 km, whereas for $T=0.58$ and onward, the applicable range is shorter, between 0.1 and 1.6 km, beyond which a scaling break is observed. At higher thresholds, only the brightest cloud regions are segmented. However, as the resolution decreases (the pixel lengths, L , increase) during the the 2×2 bilinear binning process, the bright cloud structures are averaged into apparently less bright cloud structures. This may cause these structures to fall below the brightness threshold required for segmentation. Consequently, these features may not satisfy the threshold criteria and may not be segmented or counted as they would be at higher resolutions. As a result, these bright cloud structures eventually become “undetectable” when using this thresholding method.

To understand the scaling break beyond 1.6 km, a comparison study can be carried out using a different data set that covers a larger range of resolutions. Investigating the underlying reasons for this scaling break falls beyond the scope of the current project, but can be pursued using established methods such as wavelet-based tools and 2D FFT to analyze scaling properties as well as detect scaling breaks. Relevant literature in this field includes Davis et al. (1997), Schertzer and Lovejoy et al. (1987), and Arneodo et al. (1995). These initial findings provide valuable insights into the multifractal nature of Mars clouds over the resolution range of 0.1–1.6 km.

4.3. Seasonal Variation

After examining the cloud movies and surveys obtained during the first 600 sols of the Mars2020 mission, it was observed that cloud structures in Jezero Crater were primarily detected at the beginning and end of the ACB season. Clouds were first detected on sol 64, $L_S 35.7^\circ$, during the first cloud

survey of the mission. Subsequent observations on sol 73, $L_S 39.8^\circ$ also revealed clouds (see Figure 15). The first cloud movie was captured on sol 173, $L_S 83.7^\circ$, and faint clouds were initially observed on sol 236, $L_S 111.9^\circ$, followed by a period of heightened activity with numerous cloud features between sols 279–299 ($L_S 132.1^\circ$ and 141.9°). This trend has also been reported by Toledo et al. (2023) using the Perseverance Radiation and Dust Sensor (RDS) from the Mars Environmental Dynamics Analyzer (MEDA) instrument. The cloudiest time for mesospheric clouds at Jezero Crater with the highest cloud opacities were observed between $L_S 120^\circ$ – 150° in Mars year 36.

During the ACB season at Jezero Crater between $L_S 45^\circ$ and 140° , a total of 63 cloud surveys were conducted, 11 of which ($\sim 17\%$) contained cloud sightings. Similarly, a total of 19 cloud movies were captured during the ACB season, commencing late into the season, 14 of which revealed various signs of clouds in the sky. Overall, 82 cloud observations were made, with 25 positive instances observed, which equates to approximately 30% of the measurements taken during the ACB season.

However, it is important to acknowledge that a higher incidence of cloud structures in the NavCam images does not necessarily signify peak cloudiness or high water-ice activity. Throughout the ACB season, water-ice is expected to be present in the atmosphere (Tamppari et al. 2003; Smith 2004; Wolff et al. 2019). Water-ice present in the atmosphere could be in haze form and not have definitive structures, and it might therefore be difficult to detect visually and in the MFS processing. This may be why the cloud movies between L_S values of 83.7° and 111.9° did not show cloud structures.

A possible explanation for the limited cloud sightings during the ACB season could be a sampling bias in the time of day when observations were conducted. Many NavCam

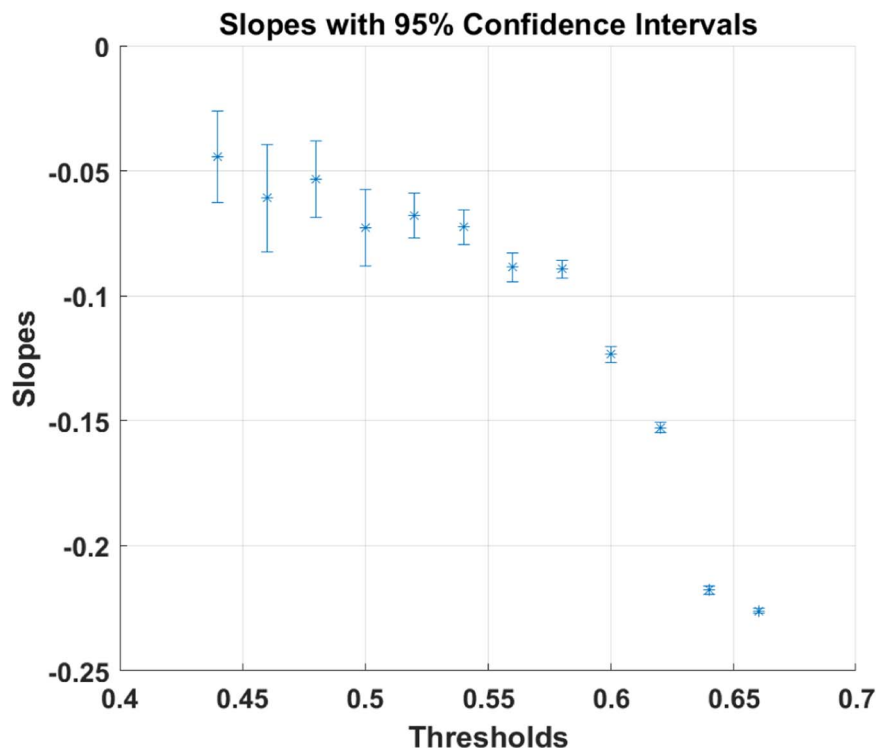


Figure 14. Slopes calculated for each threshold are plotted against the thresholds. The error bars indicate the 95% confidence intervals for each slope. The nonoverlapping confidence intervals for the higher threshold slopes indicate that these slopes are significantly different from those of the lower thresholds, providing evidence for the multifractal nature of the cloud structures.



Figure 15. Cloud survey image from sol 73, L_S 35.7°.

observations collected during the first 600 sols were obtained in the late afternoon to evening. Table 4 presents the breakdown of cloud observations based on time intervals and the corresponding percentages of cloud surveys and movies recorded during each interval. The majority of the observations occurred between 16:00 and 18:00, constituting the highest percentage of observations at 38.78%. In total, between the hours of 12:00 and 18:00, 73.47% of all observations within the initial 600 sols were recorded.

Using the Emirates Mars Infrared Spectrometer (EMIRS) on board the Emirates Mars Mission (EMM), Atwood et al. (2022) observed ACB clouds to be thicker and more widespread in the early to mid-morning compared to the mid-afternoon to early-evening period. Similarly, using the RDS on the MEDA instrument on Perseverance, Toledo et al. (2023) reported that for twilight cloud observations, 65% of the observations during sunrise contained cloud detections compared to 52% of the observations. Furthermore, the MEDA thermal infrared sensor, TIRS, has shown that atmospheric opacities during the ACB decay over Jezero during the hours when the cloud movies

Table 4
Percentages of Cloud Surveys and Cloud Movie Observations Split into Two-hour Time Periods

Time Periods (LMST)	Percentage of Cloud Survey Observations (%)	Percentage of Cloud Movie Observations (%)
04:00–06:00	1.26	0.00
06:00–08:00	4.40	2.04
08:00–10:00	12.58	12.24
10:00–12:00	15.72	4.08
12:00–14:00	23.90	10.20
14:00–16:00	15.09	24.49
16:00–18:00	25.79	38.78
18:00–20:00	1.26	4.08

were taken (Smith et al. 2023). If IR opacity is dominated by clouds, this confirms the possible bias. Because cloud surveys are single-frame images, the MFS method cannot be used to further emphasize cloud features, and therefore, fainter cloud features or hazes may not be as easily identified visually in cloud surveys as they might be in cloud movies that were processed using MFS. There is also an observational bias in the cloud movie data set. The first cloud movie collected by the Perseverance Rover was on sol 173, L_S 83.7°, which was well into the ACB season. Thus, the ability to assess early ACB cloud structures using this technique was not available during a significant part of the early ACB season. Cloud movies will be acquired more frequently during the next ACB season, providing the means to evaluate cloud occurrence as well as cloud structure characterization.

During the peak period, on sol 292, a 22° scattering halo around the Sun was also observed for around 3 hr in mid to late morning with multiple cameras on the rover, including the

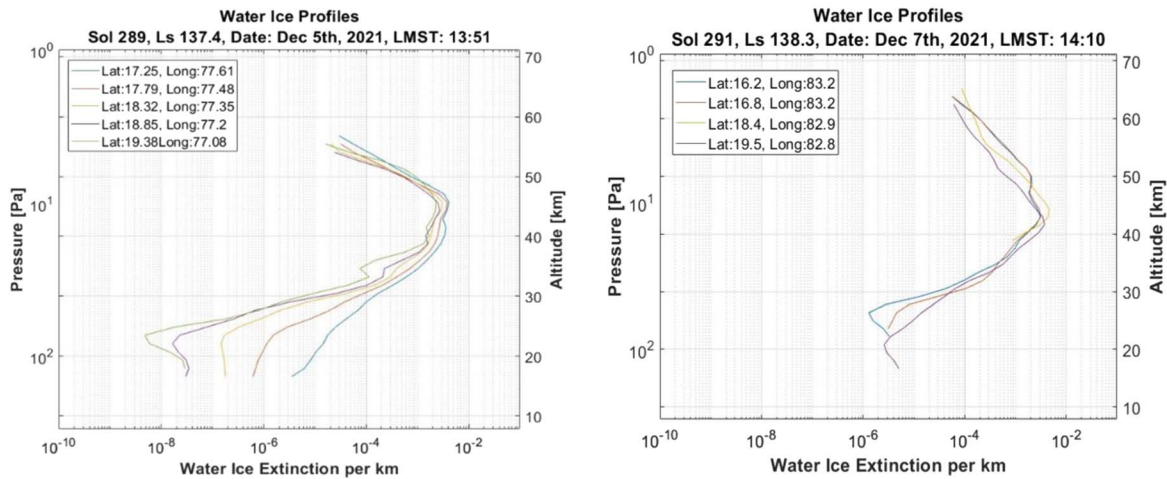


Figure 16. MCS water-ice profiles for sol 289 (left) and sol 291(right).

NavCam (Lemmon et al. 2022). The formation of such a halo requires crystalline water-ice particles up to sizes of at least $11 \mu\text{m}$ in hexagonal prisms (Bi & Yang 2014). This further provides evidence that toward the end of ACB season, a large amount of water-ice was present in the atmosphere.

Beginning with sol 313 ($L_S 153^\circ$), a regional dust storm was observed to move northward across the equator from the southwest of Jezero, which then reached the Perseverance site (Lemmon et al. 2022). Dust-lifting was seen in the NavCam images beginning with sol 313, $L_S 153.4^\circ$, along with an increase in optical depths seen until sol 318 ($L_S 156.0^\circ$; Lemmon et al. 2022). This reduced visibility of higher atmospheric activity, such as clouds. We are therefore not able to conclusively deduce when the cloud activity ended at Jezero Crater. The last observation of clouds in the first 600 sols occurred on sol 304, $L_S 144.5^\circ$.

4.3.1. Comparison with Orbiter Data: Mars Climate Sounder

To investigate the cloud altitudes and confirm the presence of water-ice clouds, we used MCS vertical profiles. The MCS instrument on board the MRO is an IR radiometer monitoring the Martian atmosphere using limb, nadir, and off-nadir viewing geometries. The MFS-processed movies containing the strongest cloud features occurred between sol 279 and sol 294. Vertical profiles of water-ice, computed using the 2D radiative transfer algorithm as described in Kleinböhl et al. (2017), were examined between $L_S 137^\circ$ and 139° over Jezero Crater between a latitude of 16° – 21° and a longitude of 67° – 87° . Nighttime and daytime MCS profiles (retrieval version 5.2) were examined during the peak cloudy period at Jezero from sol 289 to sol 292, $L_S 137^\circ$ – 139° . Since the NavCam data cover daytime, the daytime profiles that were closest to the time of the NavCam observations were used to determine the height of the clouds.

Due to rover-to-orbiter relay communication constraints, MCS is unable to observe right above Jezero Crater. Therefore, a $\pm 2^\circ$ in latitude and $\pm 10^\circ$ in longitude area around the crater is used in selecting these profiles. Furthermore, the dust in the lower atmosphere makes it difficult for MCS to probe the atmosphere below 10 km. The retrievals are oversampled and reported at a vertical resolution of typically <5 km (Kleinböhl et al. 2009, 2017).

As seen in Figure 16, the MCS sees high cloud opacity between 35 and 50 km on sol 289 and between 30 and 40 km on sol 291. The ACB clouds are generally seen between $L_S \sim 30^\circ$ and $L_S \sim 140^\circ$ around heights of 20 km and higher (Campbell et al. 2020). The NavCam clouds seen on sols 289 and 292 ($L_S \sim 137^\circ$) are likely to be what MCS data are showing as high cloud opacity between ~ 30 and 50 km. The MCS profiles further enforce the conclusion that clouds observed by NavCam during this time were most likely ACB clouds, and they aid in determining the heights at which these clouds were likely present.

4.3.2. Comparison with Orbiter Data: Emirates Exploration Imager

The Emirates eXploration Imager (EXI) is a multiband camera on board the Emirates Mars Mission (EMM), which went into orbit around Mars on 2021 February 9 (Jones et al. 2021). EXI has a resolution of 2–4 km per pixel and has six discrete bands ranging from the mid-ultraviolet to the visible. Using the “f320” UV band data, Wolff et al. (2022) have characterized the diurnal, seasonal, and spatial behavior of the ACB during Mars year 36 $L_S \sim 30^\circ$ – 190° . Specifically, the ice extinction optical depth is retrieved using similar methods to those employed by Wolff et al. (2019) in studying MARCI data on board MRO. The optical depth retrievals for MY 36 show large morning-evening asymmetries, such that the early to mid-morning times are much cloudier than mid-afternoon to early-evening periods.

The column-integrated optical depths specifically over Jezero Crater were examined using EXI data. For the retrievals, the region of interest was set at longitude 77.28° – 77.53° East and latitude 18.58° – 18.83° North. The retrieval we used does not differentiate between atmospheric and surface ice, nor between water and carbon dioxide ice. However, given the location of Jezero Crater and the seasonal time of the observation ($L_S = 30^\circ$ – 190°), the optical depth is associated with water-ice in the atmosphere (Wolff et al. 2022).

Figure 17 shows the variation in the ice extinction optical depth against sol number (specific to Perseverance) and L_S . The retrievals span from sol 79 to 500, $L_S 43^\circ$ – 267° , and from 06:00 to 18:00. The trend starts with a gradual increase in water ice, followed by a peak seen around sol 300. A drop in optical depth is seen after sol 300, when the regional dust storm occurred at Jezero Crater. This trend complements the clouds

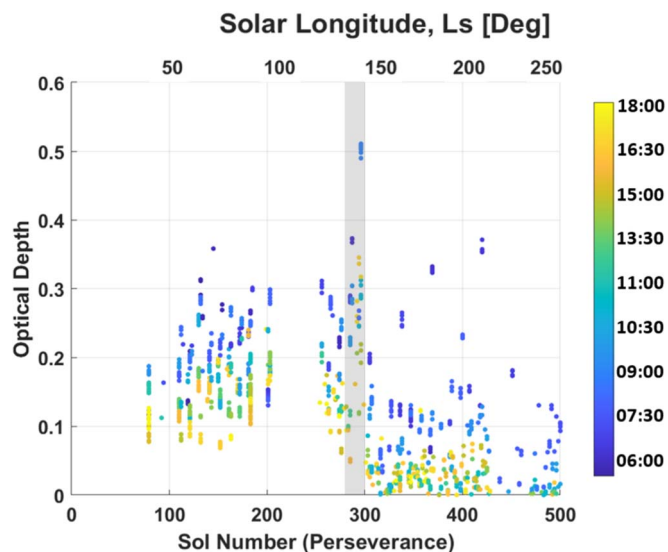


Figure 17. The ice extinction optical depth, retrieved using data from the EXI instrument on board the EMM mission, against sol number (bottom) and LS (top).

observed with NavCam data, such that the NavCam cloud movies with peak cloudiness were observed between sols 279–299 (L_S 132.1°–141.9°), shown by the gray rectangle in Figure 17. A diurnal pattern is also observed in Figure 17: the ice extinction water-ice optical depth in the morning is seen to be higher than in the evening. The highest ice extinction overall was 0.511, retrieved on sol 296 at 09:17, whereas the highest evening tau value, retrieved between 16:00–19:00, was 0.345 on sol 294 at 16:01.

During the first Mars year of observations at Jezero Crater, clouds were not observed in the NavCam cloud movies post L_S ~150. This absence does not necessarily denote a void of clouds, especially considering that clouds have been observed at Gale Crater by Curiosity all year round (Moore et al. 2015; Kloos et al. 2016; Campbell et al. 2020). The clouds observed post ACB season at Gale Crater are less frequent and optically thin. Similarly, we expect clouds at Jezero Crater, if present, to be optically thin and perhaps too faint to be discerned in the NavCam cloud movies. Furthermore, while Figure 17 does indicate afternoon optical depths over Jezero that are comparable to values retrieved over Gale Crater, it is important to highlight the distinct capabilities of the NavCam on Perseverance and the Curiosity NavCam. A comparative study of the sensitivities and capabilities of these two instruments remains beyond the scope of this paper, but is an avenue worth exploring in future work.

5. Conclusions

Over the first 600 sols of the mission, L_S 5.6°–316.8°, the Perseverance Rover collected 46 cloud movies and 145 cloud surveys using the NavCam instrument on board the Perseverance Rover. Water-ice cloud features in cloud movies were observed starting on sol 236, L_S 111.9°, followed by a peak period with many water-ice cloud features observed between sols 279–299 (L_S 132.1°–141.9°). Vertical water-ice retrievals from MCS data acquired during the same time showed that these cloud features were likely to be ACB clouds, given the timeframe and cloud altitude.

The cloud movies were analyzed further using digital image-processing techniques, 2D FFT, and thresholding (image segmentation) techniques. The statistical parameters that were successful in identifying Mars-cloud features were the standard deviation, FSC, and PPR determined using 2D FFT. The 2D FFT were also used to determine the size of the cloud structures observed at Jezero Crater, with structure sizes ranging from 2.90 to 15.25 km for cloud heights between 30 and 50 km. The resolution dependence on being able to detect these cloud structures over various thresholds was examined using the box-counting method. With this, we determined that the minimum resolution needed to detect the water-ice cloud features using the thresholding method is about 1.6 km pixel⁻¹. By computing the scaling laws at various thresholds, we showed the multifractal nature of Mars clouds seen in the resolution range of 0.1–1.6 km. This result suggests that cameras designed for tracking cloud frequency need to be able to resolve at least 1.6 km structures. Similarly, the scaling exponents may inform cloud resolving models on which two scaling laws to use at grid size resolutions lower versus higher than 1.6 km. To compute the scaling laws over other resolutions, water-ice cloud features imaged over a variety of resolutions will need to be studied using similar methods.

As the mission progresses into another Mars year, more cloudy days are expected and will be examined in upcoming studies. Future work involves using these statistical parameters to create Mars-cloud classifier algorithms, as was done with terrestrial clouds, that can recognize different types of clouds over various landing sites. Furthermore, using the projected cloud movie frames, we aim to compute wind speeds and the wind direction using the methods highlighted by Francis et al. (2014) and Campbell et al. (2021).

Acknowledgments

P.P. acknowledges the support received from a UK Science and Technology Facilities Council PhD studentship. P.P. also acknowledges and is grateful to have had the opportunity to conduct a large part of this research at the Jet Propulsion Laboratory (JPL), California Institute of Technology, under contract with the National Aeronautics and Space Administration (80NM0018D0004) and supported by the Long-Term Attachment (LTA) funding from STFC.

A.J.C and G.H.J acknowledge support from STFC Consolidated grant ST/W001004/1 to MSSL/UCL.

G.H.J.'s research was supported through the Visiting Scientist program of the International Space Science Institute (ISSI) in Bern.

Appendix

Analysis of NavCam's RGB Channels for Cloud Detection

In this study, we investigated the feasibility of using the full-color capabilities of the Navcam. Figure 18 illustrates frame 1 from sol 292, where the left panel depicts an MFS-processed frame generated using the red channel alone, and the right panel shows the frame generated using the blue channel alone. Both panels show that the red and blue channels are affected by pronounced chromatic noise, and that circular banding features are present that obscure subtle cloud details. Figure 19 shows the ratio image of the blue and red channels, which also proves to be completely unsuitable to isolating the cloud features. In contrast, Figure 20 presents an MFS-processed frame from sol

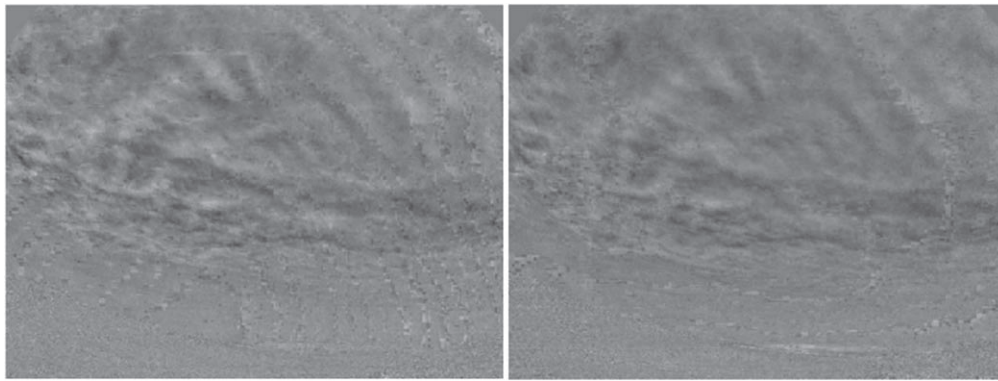


Figure 18. MFS-processed frame 1 from sol 292. The left panel was generated using the red channel and right panel using the blue channel.



Figure 19. Frame 1 from sol 292 generated by taking the ratio of the blue and red channel of the NavCam RGB image.

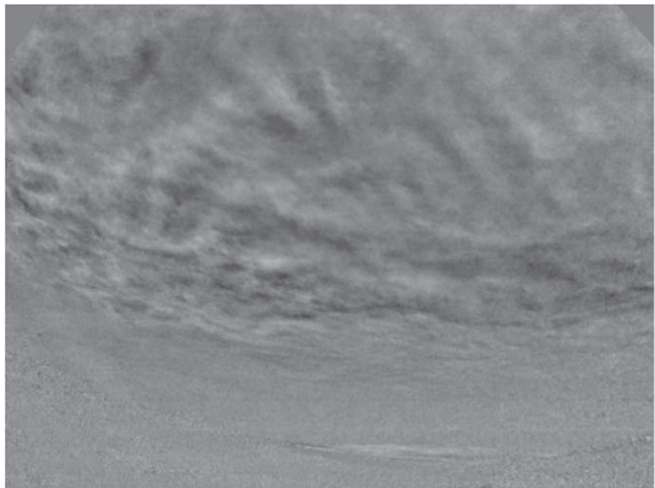


Figure 20. Frame 1 from sol 292 generated using the green-only channel.

292 generated using the green-only channel. The green channel consistently provided a clearer depiction of cloud features with minimal noise interference. While NavCam's full-color capabilities could offer broader potential for future studies, in

this specific study, the green channel proved to be the most suitable option.

ORCID iDs

Priya Patel  <https://orcid.org/0000-0001-7407-3251>
 Mark Lemmon  <https://orcid.org/0000-0002-4504-5136>
 Andrew Coates  <https://orcid.org/0000-0002-6185-3125>
 Michael Wolff  <https://orcid.org/0000-0002-1127-8329>
 Geraint Jones  <https://orcid.org/0000-0002-5859-1136>
 John Moores  <https://orcid.org/0000-0001-9435-1095>

References

- Atwood, S. A., Smith, M. D., Badri, K., et al. 2022, *GeoRL*, 49, e99654
 Apestigue, V., Gonzalo, A., Jiménez, J. J., et al. 2022, *Senso*, 22, 2907
 Arneodo, A., Bacry, E., & Muzy, J. F. 1995, *PhyA*, 213, 232
 Bi, L., & Yang, P. 2014, *JQSRT*, 138, 17
 Calbó, J., & Sabburg, J. 2008, *JATOT*, 25, 3
 Campbell, C., Kling, A., Guzewich, S., et al. 2020, *P&SS*, 182, 104785
 Campbell, C. L., Meka, S., Marrable, D., et al. 2021, *AcAau*, 181, 1
 Clancy, R. T., Wolff, M. J., & Christensen, P. R. 2003, *JGRE*, 108, 5098
 Clancy, R. T., Grossman, A. W., Wolff, M. J., et al. 1996, *Icar*, 122, 36
 Clancy, R. T., & Nair, H. 1996, *JGR*, 101, 12785
 Cooper, B., de la Torre Juárez, M., Mischna, M., et al. 2021, *JGRE*, 126, e06737
 Curran, R. J., Conrath, B. J., Hanel, R. A., et al. 1973, *Sci*, 182, 381
 Davis, A., Marshak, A., Cahalan, R., & Wiscombe, W. 1997, *JATIS*, 54, 241
 de la Torre Juárez, M., Davis, A. B., & Fetzer, E. J. 2011, *ACP*, 11, 2893
 Di, K., & Li, R. 2004, *JGRE*, 109, E04004
 Francis, R., Moores, J., McIsaac, K., Choi, D., & Osinski, G. 2014, *AcAau*, 94, 776
 Gabriel, P., Lovejoy, S., Schertzer, D., & Austin, G. L. 1988, *GeoRL*, 15, 1373
 Gennery, D. B. 2006, *Int. J. Comput. Vis.*, 68, 239
 Guzewich, S. D., Smith, M. D., & Wolff, M. J. 2014, *JGRE*, 119, 2694
 Haberle, R. M., Clancy, T. R., Forget, F., Smith, M. D., & Zurek, R. W. 2017, *The Atmosphere and Climate of Mars* (Cambridge: Cambridge Univ. Press)
 Henderson-Sellers, A. 1986, *QJRAS*, 27, 90
 Hoyt, D. V. 1978, *JApMe*, 17, 354
 Jones, A. R., Wolff, M., Alshamsi, M., et al. 2021, *SSRv*, 217, 8
 Kleinböhl, A., Friedson, A. J., & Schofield, J. T. 2017, *JQSRT*, 187, 511
 Kleinböhl, A., Schofield, J. T., Kass, D. M., et al. 2009, *JGRE*, 114, E10006
 Kleinböhl, A., Wilson, J., Kass, D., Schofield, J., & McCleese, D. 2013, *GeoRL*, 40, 1952
 Kloos, J. L., Moores, J. E., Lemmon, M., et al. 2016, *AdSpR*, 57, 1223
 Kloos, J. L., Moores, J. E., Whiteway, J. A., & Aggarwal, M. 2018, *JGRE*, 123, 233
 Lemmon, M. T., Wolff, M. J., Bell, J. F., III, et al. 2015, *Icar*, 251, 96
 Lemmon, M. T., Toledo, D., Apestigue, V., et al. 2022, *GeoRL*, 49, e99776
 Li, Q., Lu, W., & Yang, J. 2011, *JATOT*, 28, 1286
 Lovejoy, S. 1982, *Sci*, 216, 185
 Lovejoy, S., Schertzer, D., & Tsonis, A. A. 1987, *Sci*, 235, 1036
 Madeleine, J.-B., Forget, F., Millour, E., Navarro, T., & Spiga, A. 2012, *GeoRL*, 39, L23202
 Maki, J. N., Gruel, D., McKinney, C., et al. 2020, *SSRv*, 216, 137

- Mandelbrot, B. B., & Wheeler, J. A. 1983, [AmJPh](#), **51**, 286
- Martin, L. J., James, P. B., Dollfus, A., Iwasaki, K., & Beish, J. D. 1992, in Mars, ed. H. H. Kieffer et al. (Tucson, AZ: Univ. Arizona Press), 34
- Mohan, M., Bhaduri, L., & Agarwal, V. K. 1988, [InEPS](#), **97**, 159
- Montmessin, F., Forget, F., Rannou, P., Cabane, M., & Haberle, R. M. 2004, [JGRE](#), **109**, E10004
- Montmessin, F., Rannou, P., & Cabane, M. 2002, [JGRE](#), **107**, 5037
- Moore, J. E., Lemmon, M. T., Rafkin, S. C. R., et al. 2015, [AdSpR](#), **55**, 2217
- Moore, J. E., Lemmon, M. T., Smith, P. H., Komguem, L., & Whiteway, J. A. 2010, [JGRE](#), **115**, E00E08
- Otsu, N. 1979, [ITSMC](#), **9**, 62
- Smith, P. H., & Lemmon, M. 1999, [JGR](#), **104**, 8975
- Smith, M. D. 2004, [Icar](#), **167**, 148
- Smith, M. D., Martínez, G. M., Sebastián, E., et al. 2023, [JGRE](#), **128**, e2022JE007560
- Tamppari, L. K., Smith, M. D., Bass, D. S., & Hale, A. S. 2008, [P&SS](#), **56**, 227
- Tamppari, L. K., Zurek, R. W., & Paige, D. A. 2000, [JGR](#), **105**, 4087
- Tamppari, L. K., Zurek, R. W., & Paige, D. A. 2003, [JGRE](#), **108**, 5073
- Toledo, D., Gómez, L., Apéstigue, V., et al. 2023, [JGRE](#), **128**, e2023JE007785
- Wilson, R. J., Lewis, S. R., Montabone, L., & Smith, M. D. 2008, [GeoRL](#), **35**, L07202
- Wolff, M. J., Bell III, J. F., James, P. B., Clancy, T. R., & Lee, S. W. 1999, [JGR](#), **104**, 9027
- Wolff, M. J., Clancy, R. T., Kahre, M. A., et al. 2019, [Icar](#), **332**, 24
- Wolff, M. J., Fernando, A., Smith, M. D., et al. 2022, [GeoRL](#), **49**, e00477
- Xiang, P. S. 2018, [MS&E](#), **392**, 062199
- Yang, J., Lu, W., Ma, Y., Yao, W., et al. 2012, [JAOT](#), **29**, 527